J. Fluid Mech. (1997), *vol.* 340, *pp.* 395–411. Printed in the United Kingdom

The late stages of transition induced by a low-amplitude wavepacket in a laminar boundary layer

By KENNETH S. BREUER[1], JACOB COHEN[2] AND JOSEPH H. HARITONIDIS[3]

[1]Department of Aeronautics and Astronautics, MIT, Cambridge, MA 02139, USA

[2]Faculty of Aerospace Engineering, Technion, Haifa 32000, Israel

[3]Department of Aerospace Engineering, Applied Mechanics and Aviation, OSU Columbus, OH 43210, USA

(Received 14 March 1996 and in revised form 14 November 1996)

The evolution of a wavepacket in a laminar boundary layer is studied experimentally, paying particular attention to the stage just prior to the formation of a turbulent spot. The initial stages of development are found to be in very good agreement with previous results and indicate a stage in which the disturbance grows according to linear theory followed by a weakly nonlinear stage in which the subharmonic grows, apparently through a parametric resonance mechanism. In a third stage, strong nonlinear interactions are observed in which the disturbance develops a streaky structure and the corresponding wavenumber–frequency spectra exhibit an organized cascade mechanism in which spectral peaks appear with increasing spanwise wavenumber and with frequencies which alternate between zero and the subharmonic frequency. Higher harmonics are also observed, although with lower amplitude than the low-frequency peaks. The final (breakdown) stage is characterized by the appearance of high-frequency oscillations with random phase, located at low-speed 'spike' regions of the primary disturbance. Wavelet transforms are used to analyse the structure of both coherent and random small-scale structure of the disturbance. In particular, the breakdown oscillations are also observed to have a wavepacket character riding on the large-amplitude primary disturbance.

1. Introduction

The evolution of a wavepacket in a laminar boundary layer has often been proposed as an idealized model for natural, or unforced, transition to turbulence since it represents the impulse response of the boundary layer and thus includes the interactions between all frequencies and spanwise wavenumbers. The work of Gaster & Grant (1975) was one of the first detailed experiments to document the structure of the wavepacket as it evolved. By placing a hot-wire probe just outside the boundary layer (at the secondary maximum of the linear eigenfunction for u, the streamwise disturbance velocity) they were able to follow the growth of the disturbance with increasing downstream distance. Their measurements compared very well with results computed from the theoretical model of Gaster (1975) which treated the wavepacket as a summation over all spanwise wavenumbers and frequencies of least-damped linear stability eigenmodes. By computing the amplitude of each mode as it travelled

downstream, Gaster (1975) was able to reproduce both the growth and structure of the measured wavepacket during its low-amplitude phase of growth.

At their last measuring station, Gaster & Grant (1975) noted that the smooth structure of the wavepacket appeared to be breaking down and they theorized that this might have been due to nonlinear effects. This was confirmed by the measurements of Cohen, Breuer & Haritonidis (1991) who extended the work of Gaster & Grant, measuring the vertical structure of the disturbance through the boundary layer and following the evolution of the wavepacket through the nonlinear regime to its breakdown to a turbulent spot. Their results revealed that, in the linear stage, the vertical structure of each (β, ω) mode (where β is the spanwise wavenumber, and ω is the frequency) is well approximated by the least-damped linear eigenmode – a result in agreement with Gaster's (1975) model. In addition, Cohen *et al.* (1991) found that the first nonlinear interaction was characterized by the growth of a spectral peak centred about a frequency one half that of the most-amplified Tollmien–Schlichting band. The spanwise scale of the subharmonic band was found to have the same phase velocity as the primary band, suggesting that a subharmonic resonance (cf. Craik 1971; Kachanov & Levchenko 1984) was responsible for the nonlinearity. In addition, Cohen *et al.* also found that in this subharmonic stage, the linear mode shapes were still appropriate in describing the vertical structure of each wave-vector, confirming the applicability of the weakly nonlinear approach. Cohen (1994) extended Gaster's (1975) model and compared the amplitude evolution of the two and three-dimensional modes measured by Cohen *et al.* with an extended linear theory. The results indicated that the subharmonic oblique modes grew faster than predicted by linear theory, and that the growth was initiated far upstream of the Branch II locations associated with the most amplified two-dimensional fundamental waves. This added further weight to the belief that a resonant nonlinear interaction is responsible for this stage of the wavepacket's evolution. Cohen also identified a second nonlinear behaviour in which short-wavelength (high-frequency) modes started to grow at Branch II.

In the stage following the subharmonic resonance, Cohen *et al.* (1991) reported a strongly nonlinear phase in which low-frequency modes were observed to grow, as well as modes with increasing values of the spanwise wavenumber, β. In addition to the development of an increasingly complex disturbance structure, this final stage is also characterized by the appearance of small scales in the form of high-frequency oscillations. These have been observed in many transition experiments (for example, Klebanoff, Tidstrom & Sargent 1962) and are associated with the final breakdown of organized structures and the onset of random turbulent motions. The current work focuses on the late stages of the wavepacket's development with particular interest in both the spatial and spectral structure of the strongly nonlinear processes that immediately precede and subsequently announce the onset of turbulence. In order to elucidate this structure, wavelet analysis has been utilized on the instantaneous perturbation velocities.

2. Experimental details

The experiments were conducted in the closed-loop low-turbulence wind tunnel in the Department of Aeronautics and Astronautics at MIT (since moved to OSU). The facility has a test section measuring 1.22 by 0.61 m and extending 6 m in the downstream direction. For more complete details of the facility, the reader is referred to Cohen *et al.* (1991). A laminar boundary layer was established on a flat plate mounted in the test section with a free-stream velocity of $U_o = 6.65$ m s^{-1}. We define

a coordinate system with x, y and z as the streamwise, vertical (wall-normal) and spanwise directions respectively. In the x-direction the velocity is denoted by a mean component plus a perturbation, $U_o(y) + u(x, y, z, t)$, while the vertical and spanwise velocity components contain only perturbation quantities, denoted by $v(x, y, z, t)$ and $w(x, y, z, t)$ respectively. Extensive measurements of the mean flow revealed that there existed a very slight favourable pressure gradient, corresponding to a Falkner–Skan wedge-angle parameter equal to 0.01. The effect of this is minor, slightly changing the Tollmien–Schlichting growth rates from those obtained using a Blasius profile, but not altering the overall physics of the transition process.

A circular perforated plate, 1 cm in diameter, was mounted flush with the wall at $x_0 = 81$ cm (measured from the leading edge). An audio speaker was connected to the rear of the perforated plate with a short piece of flexible tubing. The speaker was weakly excited by a single period of a 24 Hz sine wave, thus exciting a low-amplitude perturbation with spectral energy concentrated at 24 Hz, and decaying as ω^{-2} for frequencies above and below $f = 24$ Hz. The frequency was chosen to match the Tollmien–Schlitching (T-S) waves whose Branch I was located at the streamwise location of the speaker. This form of disturbance excited the wavepacket (i.e. the unstable T-S modes), while keeping the transient portion of the initial disturbance (i.e. the low-frequency lightly-damped T-S modes) to a minimum. We note that, although the amplitude of the speaker excitation remained constant throughout the duration of these measurements, it is *not* the same amplitude as was used in our previous series of experiments (Cohen *et al.* 1991). Thus, the physical locations of the linear, subharmonic and breakdown stages are not the same as those in our earlier series of experiments.

All results presented here were obtained using a rake of eight hot-wire probes, measuring the streamwise component of velocity, u, through the boundary layer. The hot-wire voltages were sampled simultaneously, greatly reducing the time required for data collection and, in the breakdown region, giving an instantaneous record of the boundary layer profile. The spacing between wires was (starting with the wires closest to the wall): 1.7, 1.7, 1.7, 2.1, 2.3, 4.1 and 4.7 mm. Typically, the first wire was placed approximately 0.5 mm from the wall (the actual distance was computed from the measured mean velocity profile). Since the spacing between each hot wire was fixed, the downstream growth of the boundary layer implies that the non-dimensional location of each wire (with respect to the wall) changed with x. However, since the streamwise growth of the boundary layer is small, we were able to use the same probe at all x-locations. As an example of the non-dimensional wire spacing, at $x = 265$ cm, the eight wires were located approximately at $y/\delta^* = 0.1, 0.5, 0.8, 1.1, 1.6, 2.0, 2.8$ and 3.7. A cubic spline was used to interpolate the velocity signal to y-locations between hot-wire positions. In addition, the measured velocity data were extrapolated to $y = 0$ using the zero-slip condition at the wall, and into the far field by requiring the velocity perturbation to behave as $u \propto \exp(-\alpha y)$ as $y \to \infty$, where α is the decay rate of the least-damped T-S mode at that x-location. This provides some limited information about the flow field above the boundary layer, but given the rather crude extrapolation, these extrapolations should be regarded only as suggestive. In order to facilitate the interpretation of the results, some of the figures presented in this paper include the actual locations of the hot wires, indicated by small squares plotted along the right-hand side of the y-axis.

Measurements were performed at several x-locations downstream of the disturbance generator: $x = 170, 240, 250, 260, 265, 270, 275, 280, 282.5$ and 285 cm (measured from the leading edge). These correspond to Reynolds numbers (based on displacement

thickness) of 1494, 1775, 1812, 1847, 1865, 1883, 1900, 1917, 1926 and 1934. At each x-location, measurements were made at several spanwise locations to obtain the three-dimensional structure of the wavepacket. Since Cohen *et al.* (1991) determined that the wavepacket exhibits very good spanwise symmetry, the present experiments measured only positive values of z and symmetry was assumed in reconstructing the complete spanwise structure. For convenience in viewing the results, both positive and negative values of z are presented in the figures.

The measurement sequence was initiated by a pulse from the computer which triggered the disturbance generator. After waiting a preset delay time, $T_0 = (x - x_0)/0.935U_o$, a record of 512 points was recorded such that the total non-dimensional measuring time, $\tau = (t - T_0)U_o/(x - x_0)$, was equal to 3. This procedure is equivalent to capturing an data acquisition 'window' whose leading edge travels downstream at $0.935U_o$ and whose trailing edge travels at $0.246U_o$. The choice of these advection speeds ensured that, for each value of x, the wavepacket occupied roughly the middle third of the measurement window. At each measuring station, fifty individual events were recorded. This was more than sufficient to form a statistically meaningful ensemble average, although the procedure was aided by the use of linear de-trending.

In all the results presented, velocities have been non-dimensionalized by the free-stream velocity, U_o; length-scales (and wavenumbers) are non-dimensionalized by the local displacement thickness, δ^*. A non-dimensional frequency is also defined: $\omega = 2\pi f\delta^*/U_o$ where f is the dimensional frequency in Hz.

3. Results

3.1. *Linear and weakly nonlinear stages*

Figure 1 shows a summary of the wavepacket's downstream development. The four figures on the left show the streamwise component of velocity at $y/\delta^* = 0.5$ in the (t, z)-plane. The series of figures on the right show the corresponding two-dimensional wavenumber–frequency spectra (plotted with the non-dimensional frequency, ω, versus the spanwise wavenumber, β). The linear stage of the wavepacket is observed at $x = 170$ cm, and is characterized by the smooth swept-back wave crests and the low amplitude (approximately 0.6% of U_o peak-to-peak). The spectrum indicates that most of the energy is concentrated in the two-dimensional modes, centred about a fundamental frequency $\omega_0 = 0.09$ which corresponds to the most-amplified mode according to linear stability theory.

There is also some energy in oblique modes (the local maxima in the spectra at $(\beta, \omega) = (0.25, 0.085)$) which is reflected in the velocity contours by weak peaks on either side of the centreline. This apparent departure from the 'canonical' wavepacket of Gaster (1975) might seem to indicate nonlinear behaviour in the disturbance. However, the present results are in good agreement with the measurements of Cohen *et al.* (1991) who also measured the structure of the wavepacket inside the boundary layer and showed that the contribution to the streamwise velocity by the vertical vorticity is particularly strong inside the boundary layer, and emphasizes any energy present in oblique modes. Thus, although the oblique modes are less-amplified than the two-dimensional modes, they nevertheless may be more energetic (in the streamwise component) as a result of the relatively small amplification (or decay) of spanwise modes that are an intrinsic part of the initial disturbance generation process.

As we progress downstream, we see the onset of the first nonlinear effects. At $x = 250$ cm, oblique modes with frequency one-half that of the fundamental (i.e.

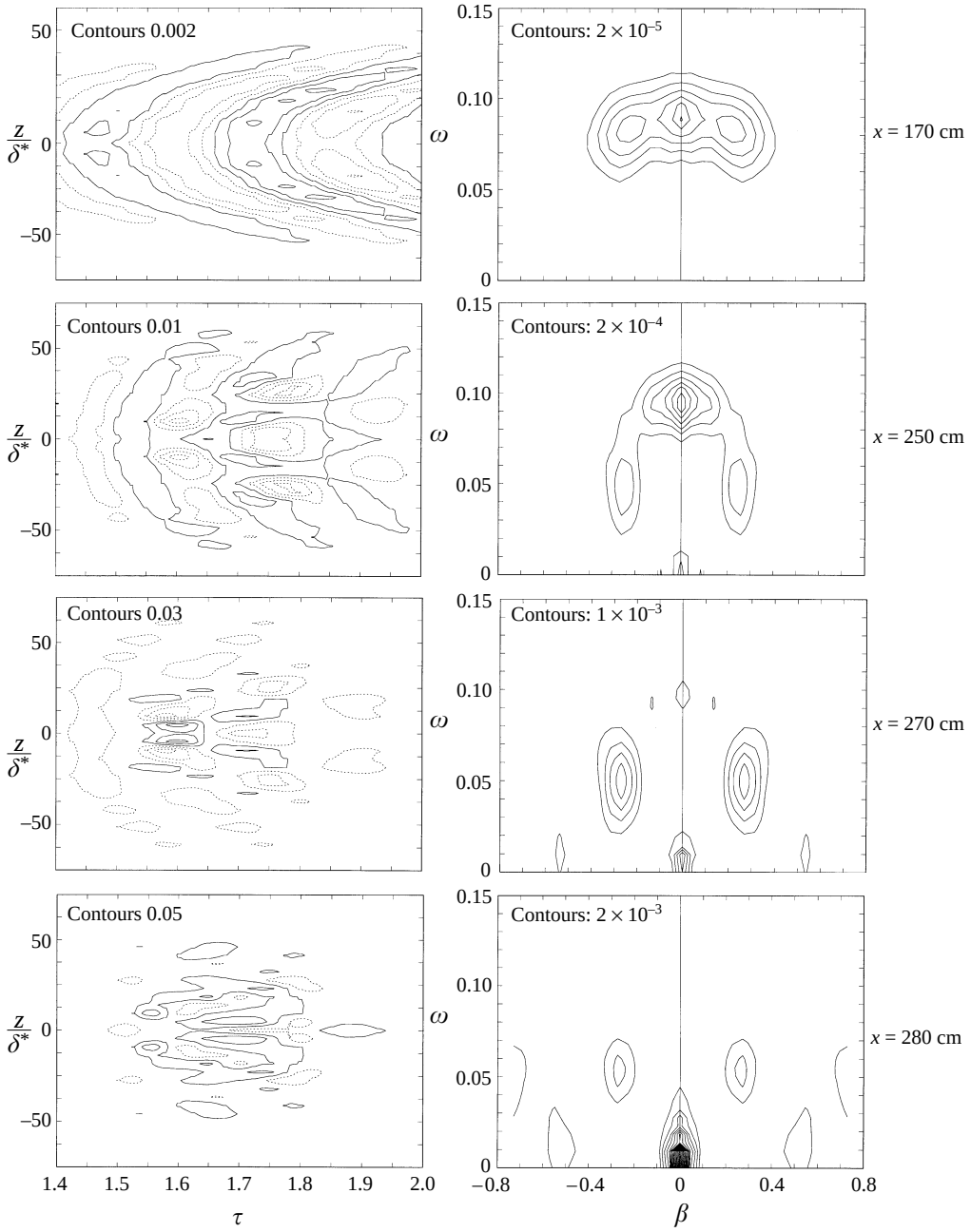

FIGURE 1. Overall view of the three stages observed during the evolution of the wavepacket. The left-hand column depicts contours of streamwise velocity perturbations, u, in the (t, z)-plane at $y/\delta^* = 0.5$. The four streamwise locations represent the linear, subharmonic, early and late breakdown stages. Solid lines show positive contour levels while dotted lines show negative levels. The right-hand column shows the corresponding wavenumber–frequency spectra of the ensemble-averaged velocity field.

subharmonic modes) gain energy, a development which is characterized by the appearance of strong peaks in the velocity perturbations on either side of the centreline. The peaks at the subharmonic ($\beta \approx 0.25$) grow out of background 'noise' and are not associated with the local oblique maxima observed at $x = 170$ cm. As with the previous stage, these results are in good agreement with the previous measurements of Cohen *et al.* (1991) and indicate that the vertical structure of each (β, ω) is still well-described by the mode shape obtained from linear stability theory. In addition, the wave speeds of the observed three-dimensional subharmonic and two-dimensional fundamental approximately satisfy a subharmonic resonance criterion. The presence of the linear mode shape and the matched wave speeds suggests that the subharmonic modes grow as part of a weakly nonlinear subharmonic resonance similar to that described by Craik (1971), or more generally, by Herbert (1988). However, the scenario is quite complex as there exist a large number of wave triads that can participate in such a resonant process since the wavepacket is described at this stage by bands of energy at both the fundamental and the subharmonic frequencies and not isolated modes as is the case for the theoretical analyses. We also observe in the spectra at $x = 250$ cm the beginning of some low-frequency, low-spanwise-wavenumber distortion of the mean flow, indicated by the small peak centred about $\beta = 0, \omega = 0$. This is a natural consequence of any nonlinear activity and is reflected in the velocity measurements as broad distortion of the Blasius flow in the wavepacket.

3.2. *Strongly nonlinear stage*

By $x = 270$ cm, the subharmonic has now overtaken the fundamental as the primary location of disturbance energy and, as figure 1 indicates, the $(0, 0)$ peak has become much more pronounced. We also see the growth of energy at $(2\beta_s, 0)$ (where β_s indicates the spanwise scale of the subharmonic peak). This is manifested in the velocity field by the appearance of strong spanwise variations, and the increasingly streaky (low-frequency, high-β) structure of the velocity perturbations. By now, the wave crests that defined the original wavepacket, although still present, are no longer visible since their amplitude is too low to appear at these contour levels.

This progression of energy to low-frequency modes continues, and at $x = 280$ cm, we see significant low-ω low-β distortion and another peak emerging at $(3\beta_s, \omega_s)$. Despite the fact that this disturbance originated from a wavepacket, the velocity field at these last two stations ($x = 270, 280$ cm) looks remarkably like the high-amplitude localized disturbances computed by Breuer & Landahl (1990) who studied the initial development of a localized disturbance in a boundary layer. Similarities are also evident between the velocity field and the numerical solutions of localized disturbances in plane Poiseuille flow computed by Henningson, Lundbladh & Johansson (1993). The propagation of energy along the β-axis is also a common feature and has been observed in the numerical simulations of localized disturbances (Breuer & Landahl 1990; Henningson *et al.* 1993).

We note that some of the higher harmonics are visible when plotted with a more sensitive contour level. Those additional peaks observed are at $(0, \omega_s)$, $(0, 3\omega_s)$, $\approx (3\beta_s, 2\omega_s)$ and $\approx (3\beta_s, 3\omega_s)$. In addition, it is important to remember that these spectra are transforms of the *ensemble-averaged* velocity field. Thus, the generation of spectral peaks which have varying or random phase will not be observed in these figures. We shall investigate one example of this immediately.

The data may be examined in a slightly different manner by plotting spectra in the (ω, y)-plane (for fixed values of x and z). This is shown in figure 2 for $z/\delta^* = 4.7$. This value of z is chosen since it represents the spanwise location which best illustrates the

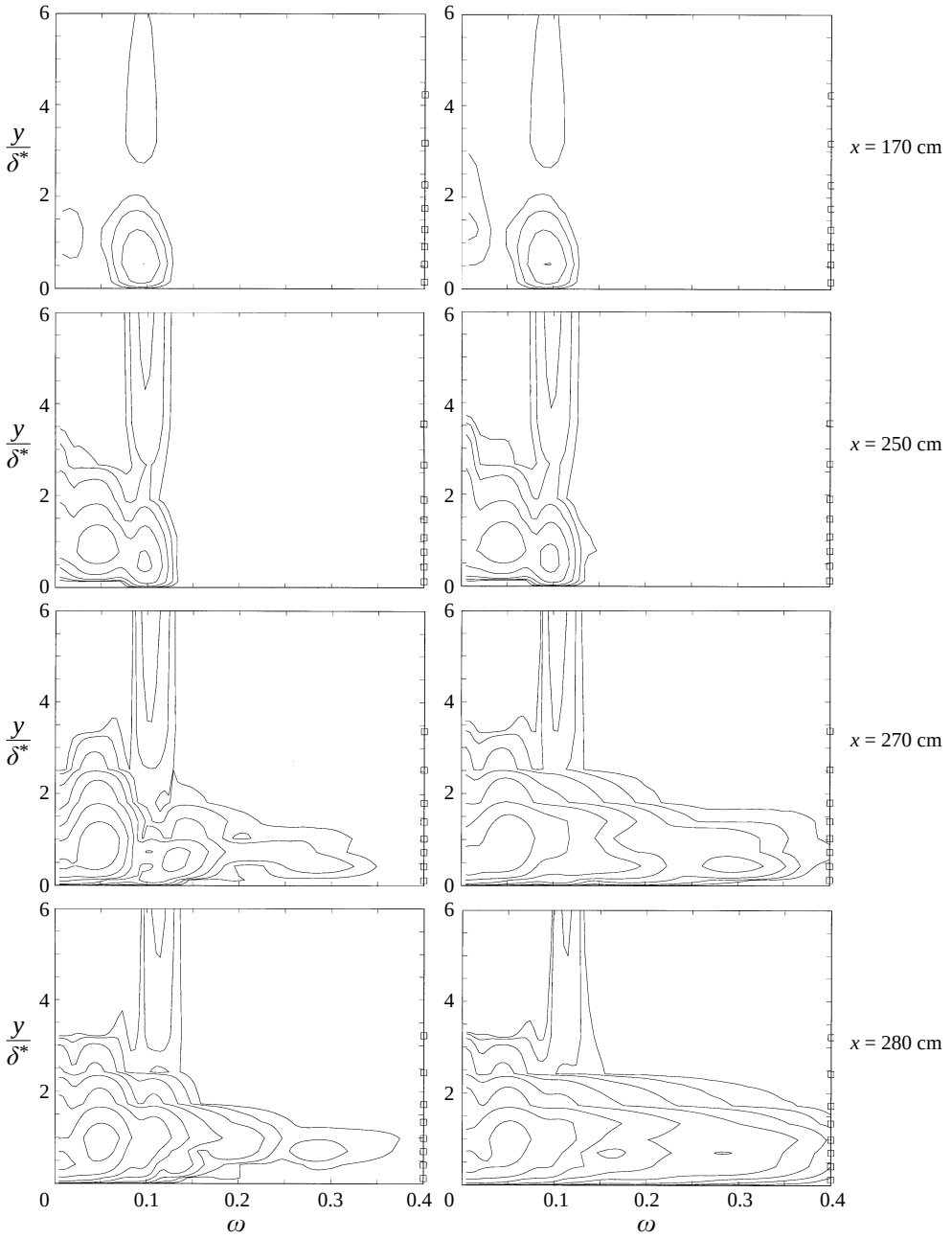

FIGURE 2. Contours of spectral power plotted in the (ω, y)-plane at $z/\delta^* = 4.7$. The left-hand column depicts the spectra of the ensemble-averaged velocities, $P(\overline{u})$, while the right-hand column shows the ensemble average of individual spectra, $\overline{P(u)}$. The contours are logarithmic, starting at 10^{-8}, with 2 contours/decade.

phenomena characteristic of this nonlinear stage. The data are plotted in two ways. If we denote as $u_i(t)$ the ith record in the ensemble, where i varies from 1 to N and N is the number of events in the ensemble, then we can compute two kinds of spectra. If we denote as $P[f(t)]$ the power spectrum of the function $f(t)$ then the left-hand column of figure 2 shows the spectra of the ensemble-averaged velocity field,

$$P[\overline{u}(t)] = P\left[\frac{1}{N}\sum_{i=1}^{N} u_i(t)\right], \tag{3.1}$$

while the right-hand column shows the ensemble average of the individual spectra,

$$\overline{P[u(t)]} = \frac{1}{N}\sum_{i=1}^{N} P[u_i(t)]\ . \tag{3.2}$$

For completely coherent signals these two will be identical and we see that for $x = 170$ and 250 cm, this is the case. At $x = 170$ we see that most of the energy is located at $\omega = 0.09$, the least-damped Orr–Sommerfeld mode at that Reynolds number. The vertical distribution also reflects the linear theory that governs this stage. The maximum occurs inside the boundary layer at approximately $y/\delta^* = 0.5$ while a second, broad maximum is observed extending into the free stream. A small peak around the zero-frequency band is also observed. This is most likely the remnant of the transient portion of the disturbance which decays quite slowly, although it might also be associated with mode–mode nonlinear interactions which, although weak at this early stage of the transition process, are nevertheless present. At $x = 250$ cm we see a similar pattern, with the exception that the energy is now also represented at the subharmonic frequency $\omega = 0.045$. The amplitude of the disturbance has also grown and the 'finger' into the free stream is stronger than before. The square symbols along the right-hand y-axis of figure 2 indicate the location of each hot wire in the boundary layer. As mentioned before, the structure above the measurement stations is obtained by extrapolating into the free stream and by requiring that the amplitude decay exponentially as $y \to \infty$. Clearly this structure is only suggestive and should be interpreted as such, but nevertheless does accurately reflect the trend of the perturbation velocity at the outer edge of the shear layer. The observed fingers stretching into the free stream thus reflect the fact that, in the narrow frequency band around $\omega = 0.1$, the perturbation amplitude is still increasing at the top of the boundary layer, while at other frequencies, it is already decaying as y increases. This behaviour is consistent with linear stability theory which indicates a secondary maximum above the boundary layer centred about the frequency of the least-damped T-S mode.

At the two later x-locations, differences begin to appear between the two types of spectra. In particular, at the higher frequencies we see that the ensemble-averaged spectra indicate much more energy located at higher values of ω than the spectra of the ensemble-averaged velocity reflect. This indicates that the scales corresponding to these frequencies are less-well correlated with the large-scale (low-frequency) portion of the disturbance and therefore tend to be smeared out by the ensemble-averaging process. However, we see that by computing the spectrum before ensemble averaging, we can capture the true spectral content of this motion which is an order of magnitude larger than the left-hand-side figures would indicate. This is especially true at $x = 280$ cm, where we see a significant amount of structure at the higher frequencies, but which has either significant phase jitter, or completely random phase. We should

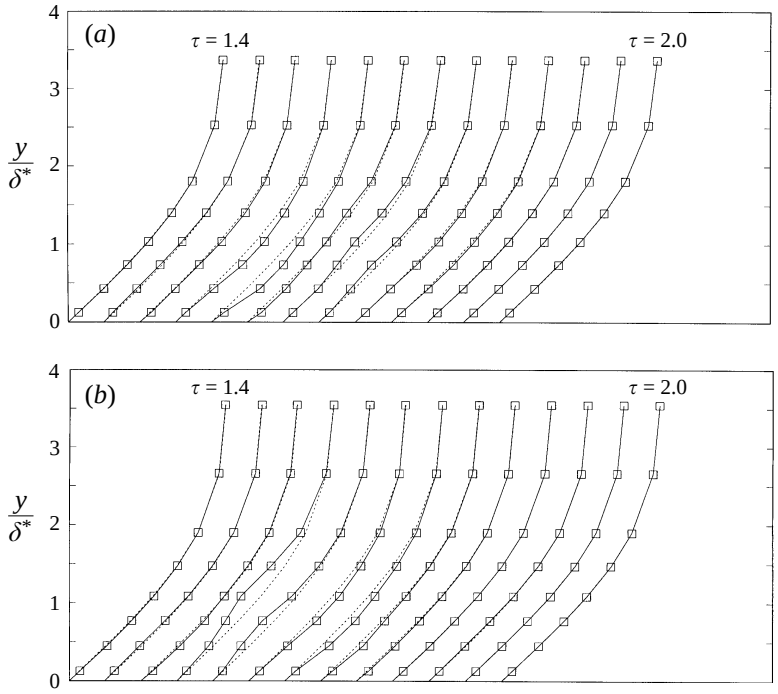

FIGURE 3. Ensemble-averaged instantaneous velocity profiles at different times, measured at $x = 270$ cm. $y/\delta^* = 4.9$ (*a*) and 9.4 (*b*). The solid lines show the phase-averaged velocity profiles (the symbols are the actual hot-wire locations) while the dotted lines show the undisturbed Blasius profile. The profiles span $\tau = 1.4 - 2.0$ in increments of 0.05.

note that phase jitter results from small differences in the structure and arrival time of individual events (due to variations in the mean flow, disturbance generator, etc). Large-scale structures (i.e. low frequencies) are not adversely affected by this jitter. However, the effect of small variations in t becomes important at higher frequencies and the ensemble average tends to smear out the small-scale structure. Thus, the observed differences between $P[\overline{u}]$ and $\overline{P[u]}$ at $x = 270$ and $x = 280$ cm does not necessarily mean that the high-frequency motion has random phase. It may be perfectly correlated with the large-scale motion, but be smeared out by small variations in the arrival time of each event.

3.3. *Distortion of local mean profile*

As figure 1 indicates, by $x = 270$ cm, the disturbance has grown to a substantial amplitude, and the wavenumber–frequency spectrum indicates that distortion (at $\omega \approx 0, \beta \approx 0$) has become quite significant. At this stage, the disturbance amplitude is sufficiently large that the instantaneous velocity profiles are significantly distorted from Blasius. This is illustrated in figure 3, which shows ensemble-averaged instantaneous velocity profiles plotted for $\tau = 1.4$ to $\tau = 2.0$ in increments of 0.05. Here, we plot the velocity profiles at two spanwise locations: $z/\delta^* = 4.7$ and 9.4. These represent the central portion of the disturbance, where a high-speed region of fluid is followed by a low-speed region, and the off-centre portion of the disturbance, where the converse occurs. Both show strong distortion. In the regions of locally accelerated fluid ($z/\delta^* = 4.7$ at $\tau \approx 1.6$ and $z/\delta^* = 9.4$ at $\tau \approx 1.7$) the profiles are fuller while in the regions of locally decelerated flow ($z/\delta^* = 4.7$ at $\tau \approx 1.7$ and $z/\delta^* = 9.4$ at $\tau \approx 1.55$),

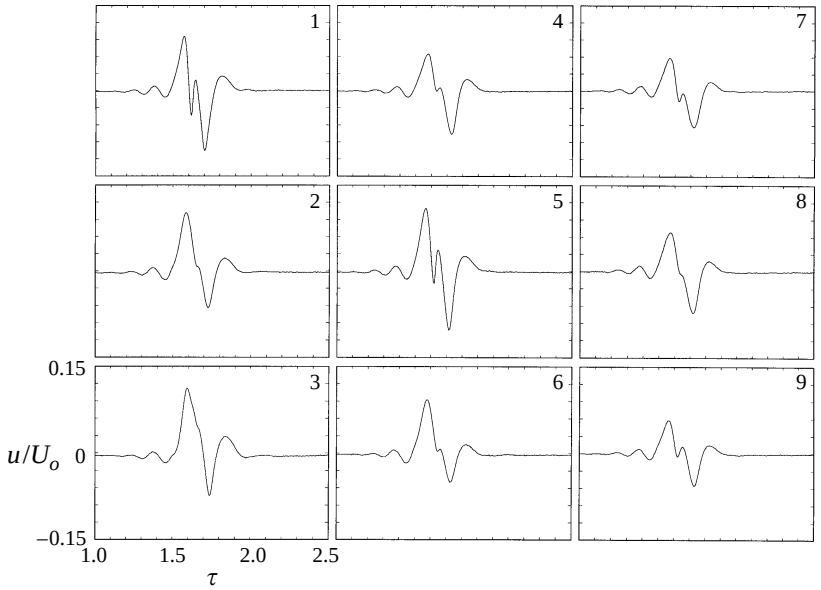

FIGURE 4. Plots of u/U_o vs. τ for nine individual realizations (events) at $x = 270$ cm, $z/\delta^* = 4.7$ and $y/\delta^* = 0.75$.

the profiles have become inflectional. This immediately alerts us to the possibility of localized breakdown due to Rayleigh instabilities associated with these inflectional instantaneous profiles. However, one must remember that an inflection point in the vertical direction does not guarantee breakdown, and that in this complex disturbance field it is likely that there exists a significant spanwise velocity field and both spanwise and streamwise gradients in all three velocity components.

3.4. *Small-scale structure and higher harmonics*

The presence of energy at high frequencies, shown in figure 2, suggests that the ensemble-averaged signals have lost some significant information at the latter stages of the disturbance growth. As mentioned above, while small variations in the structure and arrival time of each event will not adversely affect the ensemble-averaged structure at the large scales, they will smear out small-scale structure. Thus, in order to explore this small-scale structure, we must look at individual events.

Velocity traces from one of the hot wires, at $x = 270$ cm, $y/\delta^* = 0.75$ and $z/\delta^* = 4.7$ are shown in figure 4. Here, nine individual events are represented. At first glance we see that the coherence of the events is, in general, quite good and that, despite the high levels of perturbation from the undisturbed mean (approximately 25% of U_o, peak-to-peak), both the shape and amplitude of the disturbances are consistent from one event to the next. At this location we are looking at the passage of a region of increased normal shear, indicated by the initial region of accelerated fluid, followed by a region of decelerated fluid. What is interesting here, however, is the 'kink' in the velocity signal at the centre of the transition from high- to low-speed fluid. Although there are some variations in intensity, this kink is detectable in every event. Unlike the large-scale structure, this feature of the flow is not perfectly repeatable and because both its strength and position (in both time and space) vary slightly between events, it is smeared out by the ensemble-averaging procedure. By measuring the period of the kink, we can estimate its frequency to be approximately $\omega = 0.26$ which is in

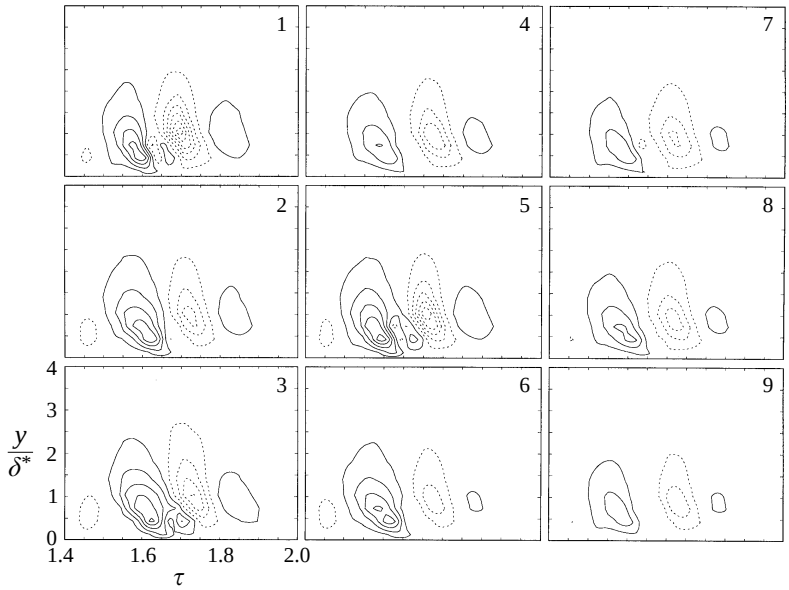

FIGURE 5. Contours of streamwise perturbation velocity at $x = 270$ cm, $z/\delta^* = 4.7$ showing the growth of small-scale structure during the latter stages of transition. The individual events shown here are the same ones used in figure 4. Contour levels: 0.025 U_o. Solid lines depict positive values while dotted lines show negative values.

reasonable agreement with the observed peak at $\omega = 0.3$ indicated by the spectra at the same spanwise location (figure 2).

Since the data were taken using a boundary layer rake, we can also plot the instantaneous contours of u at $x = 270$ cm, $z/\delta^* = 4.7$. This is shown in figure 5, using the same events as in figure 4. For some of the events, the kink that was observed in the velocity signal is not evident (a reminder that contour plots can obscure important detail). However, events 1, 3 and 5 in particular clearly show the development of small-scale structure in the lower portion of the disturbance, below $y/\delta^* = 1.0$. These events correspond to the frames in figure 4 which showed a well-developed kink in u, and are also the events with stronger large-scale structure. Re-plotting figure 5 with a finer contour spacing reveals that, for all events, these 'islands' between the two large-scale structures exist, although they have much lower amplitude in the weaker events: 2, 4, etc. A comparison between the rendering of event 3 in figures 4 and 5 also illustrates that the absolute location of the kink with respect to the wall is somewhat variable (compare, for example, events 1 and 3).

3.4.1. *Wavelet analysis*

In attempting to isolate the small-scale structure for further analysis, one is tempted to remove the large-scale structure by using a high-pass filter. This was tried but the results were somewhat inconclusive since there does not exist a clear separation between the large and small scales in frequency space. In fact, the rapid change of u with time shown in figure 4 implies that there are high frequencies associated with the large-scale shear, $\partial u/\partial\tau$, which will not, in general, be separable from the high-frequencies associated with the small-scale kinks in u. This difficulty has been noted before by Kachanov (1987) who demonstrated that the frequency, amplitude and phase of filtered signals are extremely sensitive to the details of the filter and the

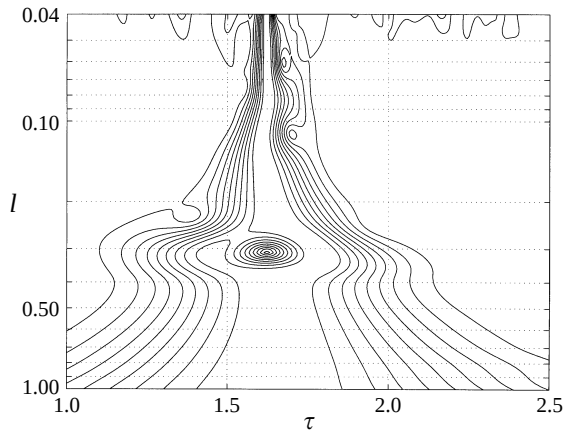

FIGURE 6. Contour plot showing the distribution of the wavelet transform coefficients as functions of τ and the wavelet dilation parameter, l. The signal analysed here is event 1 from figure 4.

choice of the cutoff frequency. However, the use of a wavelet transform can reveal some of this structure without the uncertainties of simple time-series filtering. This was applied with some promise to transitional boundary layer flows by Shaikh & Gaster (1994) and has the advantage over simple filtering of retaining the temporal structure of the velocity signal at each filtered scale.

For the current analysis, we have utilized the continuous wavelet transform (for a comprehensive discussion of wavelet applications in fluid mechanics, see Farge 1992) in which the wavelet coefficients $\tilde{u}(\tau; l)$ for each dilation scale, l, are defined by the convolution integral:

$$\tilde{u}(\tau; l) = \int u(\tau')\psi\left(\frac{\tau' - \tau}{l}\right) \mathrm{d}\tau' \tag{3.3}$$

where $\psi(x)$ is the wavelet function, in this case chosen to be the complex Morlet wavelet:

$$\psi(t) = \mathrm{e}^{\mathrm{i}k_\psi t}\mathrm{e}^{(-|t|^2/2)}, \tag{3.4}$$

and k_ψ is chosen to have a value of 6 in accordance with the recommendation by Farge (1992). In the applications presented here, the dilation parameter l was varied from 0.02 to 1.0, a range that was established empirically and found to cover the complete range of interesting features observed in the experimental velocity signals.

Figure 6 shows the distribution of the wavelet coefficients, $\tilde{u}$, resulting from a continuous wavelet expansion of event 1 from figure 4. In keeping with the customary presentation of wavelet transform data, the coefficients corresponding to large values of l (representing large scales) are plotted at the bottom of the figure while small values of l, representing small scales, are plotted at the top of the figure. Since the primary purpose is to reveal the presence of small-scale structure, we have adopted the common procedure (Farge 1992) of normalizing the wavelet coefficients by their maximum at each scale, l. This allows a clear visualization of structure at different scales although information regarding relative amplitudes has been discarded. The transform, however, clearly illuminates the appearance of the kink, represented by the peak in the contour plot at $(\tau, l) = (1.6, 0.3)$. The difficulty with time-series filtering is also highlighted by the sharp peak at $\tau = 1.6$ that continues into the small scales (i.e low values of l, at the top of the figure). This is clearly associated with the steep

deceleration in the velocity signal (figure 4) and would be retained in a conventional high-pass time-domain filtering process.

It is unclear whether or not the velocity kinks revealed in the individual events by figures 4, 5 and 6 represents an instability wave growing on the locally distorted velocity field and would be visible in a contour plot by waviness or kinks in the velocity contours. In addition, at this stage of the transition process in which we see significant distortion of the instantaneous velocity profiles, one would expect that inflectional and secondary instabilities would not be difficult to excite. However, one must proceed with caution. On comparing the distorted mean profiles (figure 3) with the individual contour plots (figure 5), one sees that the location of the velocity kinks falls between a region with a stabilized profile on the upstream end and a destabilized profile on the downstream end of the disturbance. In addition, the phase of the kink (with respect to the large-scale features of the disturbance) is quite repeatable. Since an instability would typically be associated with a destabilized (inflectional) profile and would not exhibit such repeatable phase, it would therefore seem that this small-scale feature is not due to an instability phenomenon. Rather it appears to be the first sign of higher harmonics due to nonlinear effects or, perhaps, a resonant interaction (Kachanov 1994).

Although the wavenumber–frequency spectra (figure 1) indicate that the dominant transfer of energy is towards low-frequency high-spanwise-wavenumber scales, the previous results (figure 4) illustrate the first appearance of a higher-harmonic feature. As the wavepacket continues to evolve, more complex high-frequency features are also observed, although they can only be seen in individual events. Since the data were acquired with a boundary layer rake, frequency spectra as a function of ω and y are available from each individual event. Four such events are shown in figure 7 chosen from four x-stations in the subharmonic and breakdown regimes.

These spectra illustrate the progression of the spectrum without any averaging to smear out fine details. At $x = 265$ cm, the basic linear and subharmonic structures are observed (as discussed earlier). This is intensified at $x = 275$ cm and we also see the appearance of the coherent small-scale structure at $\omega = 0.35$ and manifested as the kink in the velocity time-series. At $x = 280$ and 282.5 cm, we see the cascade of energy to high frequencies. Note that the contour levels here are logarithmic (one contour for each half-decade) so that the higher frequencies have significantly lower energy. Nevertheless, the structure of nonlinear interactions generating a series of higher harmonics is evident. Recent work by Healey (1995) has revealed a mechanism for the resonant growth of higher harmonics in a boundary layer. Although we have not attempted to verify this mechanism quantitatively, it warrants careful consideration as a possible explanation for the growth of selected higher frequencies observed in the present data.

3.5. *Onset of breakdown*

Once energy is available at high frequencies, it is likely to be rapidly amplified since the instantaneous velocity profiles, now highly distorted, are inflectional and thus inviscidly unstable. This scenario is supported by the observation that, after $x = 282.5$ cm, the individual traces become less repeatable and the wavepackets begin to break down to turbulent spots. Examination of individual realizations indicates that while some of the disturbances are still 'laminar', some were observed to contain high-frequency content with random phase, indicating their breakdown to a chaotic state. Other events were clearly undergoing breakdown and showed the presence of a breakdown instability, still in infancy. An example of this stage is presented in figure 8

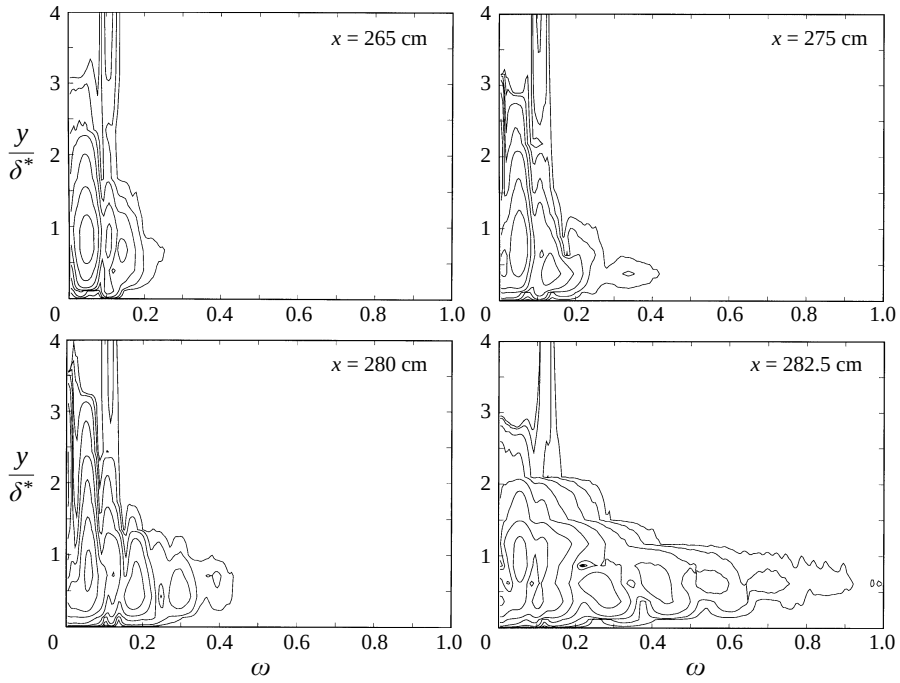

FIGURE 7. Representative frequency spectra, plotted vs. y at different x-locations illustrating the generation of harmonics during the breakdown stage. $z/\delta^* = 4.7$. Logarithmic contour levels plotted in half-decades.

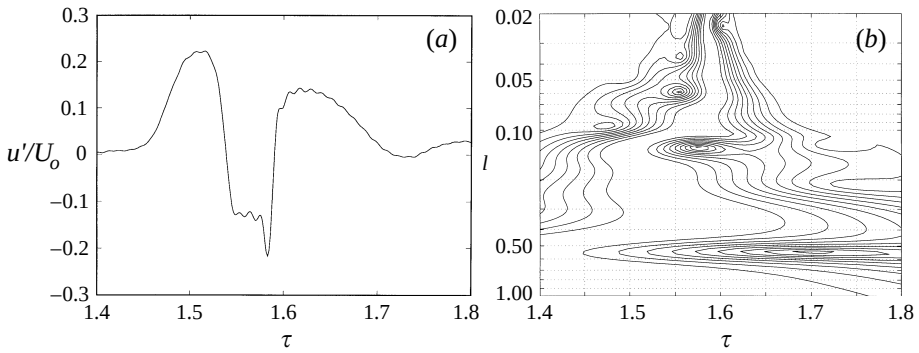

FIGURE 8. Streamwise velocity signal (a) and its corresponding wavelet transform (b). $x = 285$ cm, $y/\delta^* \sim 1$, $z/\delta^* = 9.4$.

which shows a single streamwise velocity signal at $x = 285$ cm, $y/\delta^* \approx 1$. Figure 8(a) shows the full velocity perturbation while figure 8(b) shows the corresponding wavelet transform, as defined in §3.4.1.

As before, each 'peak' in the wavelet amplitude contour plot can be identified with a feature of the original velocity signal. In particular, a discrete peak at $l = 0.06$, $\tau \approx 1.55$ is present in some of the individual realizations and appears to be associated with small-amplitude high-frequency oscillations leading to the breakdown to turbulence. Although the phase and amplitude of each individual event differ, this example is representative of the entire data set. An estimate of the vertical

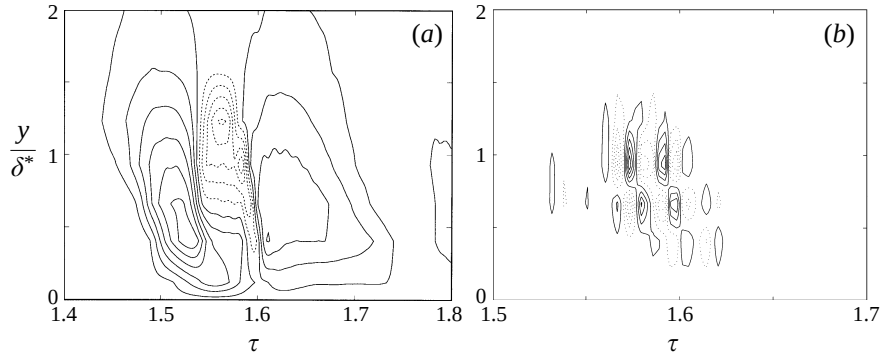

FIGURE 9. Contours of streamwise perturbation velocity: (*a*) full signal with no filtering; (*b*) the wavelet-transformed signal at a single dilation scale of $l = 0.06$. For this case, no wavelet coefficient normalization was performed. $x = 285$ cm, $z/\delta^* = 9.4$. Contour levels: $0.05U_o$ (*a*) and $0.01U_o$ (*b*).

structure of the same event is shown in figure 9 in which case we have taken the wavelet transform of each hot-wire signal with a single dilation parameter of $l = 0.06$ and re-constructed the t–y 'filtered' velocity signature. Unlike the previous examples of the wavelet transform, the wavelet coefficients are not normalized and thus the amplitudes of the small-scale structure can be compared with those of the full signal. As before, the full structure is plotted in part (*a*) while the filtered disturbance is plotted in part (*b*) (Note the change in scale on the filtered figure.) In both cases, the temporal resolution of the digitized data is somewhat marginal and so there may be additional high-frequency features which have not been captured accurately. In addition, the difficulties associated with time-series filtering (Kachanov 1987) should be kept in mind when interpreting these data. Specifically, we must emphasize that, even though the wavelet does indicate a small peak at $l = 0.06$, there is not a clear scale separation as was observed in figure 6. Nevertheless, the basic structure of the breakdown is clear and we note that, although the frequency of the observed 'breakdown oscillations' does vary somewhat with l, the structure and amplitudes indicated by figure 9 are quite robust to moderate changes in the selected dilation parameter, l. It is interesting to note that the maximum amplitude of the secondary wavepacket is located in the narrow low-speed region of the primary perturbation (just ahead of $\tau = 1.6$) and that the high-frequency structure is inclined to the left at the same angle as the large-scale inclination. This low-speed region is analogous to the classic 'spike stage' observed by Klebanoff *et al.* (1962).

4. Discussion and conclusions

The results presented here illustrate some of the details of the nonlinear phase of transition, and the ultimate breakdown to turbulence. Three distinct phases can be identified: a subharmonic stage, strong nonlinear stage resulting in the progression of energy with zero or low frequency to increasingly small spanwise scales and, to a lesser extent, in the generation of higher harmonics. Lastly we observe the appearance of high frequencies with random phase riding on intense shear layers in the disturbed flow.

The subharmonic stage is in good agreement with previous experiments (Gaster & Grant 1975; Cohen *et al.* 1991; Cohen 1994) and at this point seems well-understood. The next stage – the generation of low-frequency high-spanwise-wavenumber modes

– may also be understood as a direct consequence of nonlinear mode interactions. The preference for low-frequency modes has been observed in numerical experiments (Pruett & Zang 1992; Kim & Moser 1989) and has been discussed in some detail by Henningson *et al.* (1993) who attribute this '*β-cascade*' to a two-stage process. In the first stage, 'seed' energy is first generated by nonlinear mode interactions while the second stage serves to amplify this seed energy via a transient growth mechanism (cf. Landahl 1980; Gustavsson 1991; Henningson, Gustavsson & Breuer 1994) in which a small amount of energy concentrated primarily in the v-component is rapidly amplified by a linear interaction with the mean profile which generates vertical vorticity due to vortex tilting and stretching by the strong mean shear. The mechanism has a strong preference for low-frequency modes since these exhibit the most dramatic transient amplification (see, for example Breuer & Kuraishi 1994). In the present configuration, the subharmonic oblique energy peak, $(\pm\beta_s, \omega_s)$, interacts nonlinearly with the fundamental, $(0, 2\omega_s)$, to generate seed energy at $(\pm 2\beta_s, 0)$ which then grows through a transient growth mechanism. This process continues resulting in the progression of energy along the β-axis. Although higher harmonics are also created by nonlinear mode interactions, they are less energetic since they are not amplified by the transient growth to the same degree as the low-frequency modes. Although there is no conclusive proof that this transient-assisted nonlinear mechanism is the root cause for the observed development, these theoretical considerations do provide considerable support for the current results, and although this has been observed numerically as described above, we believe it to be the first experimental confirmation of this aspect of the transition process.

High-frequency modes are also generated by mode interactions and are observed in the present results, albeit at lower amplitudes. However, the generation of the higher harmonics is reflected in the velocity signals by very intense streamwise gradients. The generation of these narrow regions of low-speed fluid is in accordance with the 'spike' stage of Klebanoff *et al.* and with the results of Henningson *et al.* (1993) who observed a rapid growth in v which lifts up low-speed fluid from the wall. It is at these locations that we observe the growth of high-frequency instabilities with random phase which lead directly to turbulence. The wavelet analysis techniques used here have proved to be quite effective in delineating the spatial and spectral structure of these complex signals. Related measurements by Gaster (1991) show a similar route to turbulence in which high-frequency oscillations are observed on a finite-amplitude shear layer induced by the primary disturbance (in Gaster's case, a point-harmonic source). Gaster reported that the secondary waves have frequency of about 5 to 6 times that of the primary frequency. This value is slightly lower than the ratio of about 7 found in the present results but can be considered comparable given the difficulties discussed regarding high-pass filtered time series. The complexity of the disturbance at this late stage of transition makes the complete analysis extremely difficult. Ideally one would have data on more than one velocity component and simultaneous measurement in z as well as in y. However, despite these shortcomings, the results presented here are consistent with related numerical experiments and with physical intuition.

While these two breakdown mechanisms (the β-cascade and the appearance of high frequencies at the spike regions) may be universal to all three-dimensional flows, what will differ between the two disturbances is the spatial and temporal scales on which they evolve. For example, in the present results, the primary three-dimensional scale is determined from the conditions that meet the criteria for the subharmonic resonance. In contrast, the three-dimensionality that evolves from an initially two-

dimensional disturbance (such as a ribbon-induced two-dimensional T-S wave) might have a different scale. (The spanwise wavenumber forced by Klebanoff *et al.* had a spanwise wavenumber of approximately 0.42 compared with 0.3 in the present case.) Given this, one might expect that, even if the underlying nonlinear mechanisms are identical, their relative strengths and characteristic scales will be different. Similarly, an initially three-dimensional localized disturbance will have length scales which are imposed by the nature of the initial perturbation. Again, one might expect the physics of the breakdown process to be similar to the results presented here although the details may differ.

REFERENCES

Breuer, K. S. & Kuraishi, T. 1994 Transient growth in two- and three-dimensional boundary layers. *Phys. Fluids* **6**, 1983–1993.

Breuer, K. S. & Landahl, M. T. 1990 The evolution of a localized disturbance in a laminar boundary layer. Part 2. Strong disturbances. *J. Fluid Mech.* **220**, 595–621.

Cohen, J. 1994 The initial evolution of a wave-packet in a laminar boundary layer. *Phys. Fluids* **6**, 1133–1143.

Cohen, J., Breuer, K. S. & Haritonidis, J. H. 1991 On the evolution of a wave packet in a laminar boundary layer. *J. Fluid Mech.* **225**, 575–606.

Craik, A. D. D. 1971 Nonlinear resonant instability in boundary layers. *J. Fluid Mech.* **50**, 393–413.

Farge, M. 1992 Wavelet transforms and their applications to turbulence. *Ann. Rev. Fluid Mech.* **24**, 395–451.

Gaster, M. 1975 A theoretical model for the development of a wave packet in a laminar boundary layer. *Proc. R. Soc. Lond.* A **347**, 271–289.

Gaster, M. 1991 On the origins of turbulence. (Unpublished manuscript).

Gaster, M. & Grant, I. 1975 An experimental investigation of the formation and development of a wave packet in a laminar boundary layer. *Proc. R. Soc. Lond.* A **347**, 253–269.

Gustavsson, L. H. 1991 Energy growth of three-dimensional disturbances in plane Poiseuille flow. *J. Fluid Mech.* **224**, 241–260.

Healey, J. J. 1995 A new boundary layer resonance enhanced by wave modulation: theory and experiment. *J. Fluid Mech.* **304**, 231–262.

Henningson, D. S., Gustavsson, L. H. & Breuer, K. S. 1994 Localized disturbances in parallel shear flows. *J. Appl. Res.* **53**, 51–97.

Henningson, D. S., Lundbladh, A. & Johansson, A. V. 1993 A mechanism for bypass transition from localized disturbances in wall-bounded shear flows. *J. Fluid Mech.* **250**, 169–207.

Herbert, T. 1988 Secondary instability of boundary layers. *Ann. Rev. Fluid Mech.* **20**, 487–526.

Kachanov, Y. S. 1987 On the resonant nature of the breakdown of a laminar boundary layer. *J. Fluid Mech.* **184**, 43–74.

Kachanov, Y. S. 1994 Physical mechanisms of laminar boundary layer transition. *Ann. Rev. Fluid Mech.* **26**, 411–482.

Kachanov, Y. S. & Levchenko, V. Y. 1984 The resonant interaction of disturbances at laminar turbulent transition in a boundary layer. *J. Fluid Mech.* **138**, 209–247.

Kim, J. & Moser, R. 1989 On the secondary instability in plane Poiseuille flow. *Phys. Fluids* A **1**, 775–777.

Klebanoff, P. S., Tidstrom, K. D. & Sargent, L. M. 1962 The three-dimensional nature of boundary layer instability. *J. Fluid Mech.* **12**, 1–34.

Landahl, M. T. 1980 A note on an algebraic instability of inviscid parallel shear flows. *J. Fluid Mech.* **98**, 243–251.

Pruett, C. D. & Zang, T. A. 1992 Direct numerical simulation of laiminar breakdown in high speed axi-symmetric boundary layers. *AIAA Paper* 92-0742.

Shaikh, F. N. & Gaster, M. 1994 The non-linear evolution of modulated waves in a boundary layer. *J. Engng Maths* **28**, 55–71.